Spectroscopic observation of SU(*N*)-symmetric interactions in Sr orbital magnetism

X. Zhang *et al.*

Science **345**, 1467 (2014);
DOI: 10.1126/science.1254978

RESEARCH ARTICLES

QUANTUM SIMULATION

Spectroscopic observation of SU(*N*)-symmetric interactions in Sr orbital magnetism

X. Zhang,[1,2] M. Bishof,[1,2] S. L. Bromley,[1,2] C. V. Kraus,[3,4] M. S. Safronova,[5,6] P. Zoller,[3,4] A. M. Rey,[1,2]* J. Ye[1,2]*

SU(*N*) symmetry can emerge in a quantum system with *N* single-particle spin states when spin is decoupled from interparticle interactions. Taking advantage of the high measurement precision offered by an ultrastable laser, we report a spectroscopic observation of SU($N \leq 10$) symmetry in ^{87}Sr. By encoding the electronic orbital degree of freedom in two clock states while keeping the system open to as many as 10 nuclear spin sublevels, we probed the non-equilibrium two-orbital SU(*N*) magnetism via Ramsey spectroscopy of atoms confined in an array of two-dimensional optical traps; we studied the spin-orbital quantum dynamics and determined the relevant interaction parameters. This study lays the groundwork for using alkaline-earth atoms as testbeds for important orbital models.

Symmetries play a fundamental role in the laws of nature. A prominent example is the SU(3) symmetry of quantum chromodynamics, which governs the behavior of quarks and gluons. When generalized to large *N*, SU(*N*) is expected to generate exotic many-body behaviors emerging from the increased degeneracy and strict conservation laws. Owing to the strong decoupling between the electronic-orbital and nuclear-spin degrees of freedom (*1*, *2*), alkaline-earth atoms and others with similar structure prepared in the two lowest electronic states (clock states with zero electronic angular momenta) are predicted to exhibit nuclear spin (*I*) independence for their interatomic collisional parameters. This property directly leads to a SU($N \leq 2I + 1$) symmetry for the interaction physics (*3*–*6*). Thanks to this symmetry, in addition to their use as ideal timekeepers (*7*) and quantum information processors (*8*–*11*), alkaline-earth atoms are emerging as a unique platform for the investigation of high-energy lattice gauge theories (*12*); for testing of orbital models used to describe transition metal oxides, heavy fermion compounds, and spin liquid phases (*13*); and for the observation of exotic topological phases (*6*, *14*). Progress toward these goals includes the production of quantum degenerate alkaline-earth gases (*15*–*17*), imaging of individual spin components (*18*), control of interactions (*16*, *19*, *20*), and study of many-body spin dynamics (*21*).

Thus far, only indirect evidence for SU(*N*) symmetry exists (*22*), including inference from suppressed nuclear spin-relaxation rates (*18*), reduced temperatures in a Mott insulator for increased numbers of spin states (*23*), and the changing character of a strongly interacting one-dimensional fermionic system as a function of *N* (*24*). Furthermore, these observations are limited to the electronic ground state. The corresponding ground-state *s*-wave scattering parameter a_{gg} has been determined from photoassociation (*25*) and rovibrational spectroscopy (*26*), but the excited state–related scattering parameters remain undetermined.

Here, we report a spectroscopic observation of SU(*N*) symmetry and two-orbital SU(*N*) magnetism in an ensemble of fermionic ^{87}Sr atoms at microkelvin temperatures and confined in an array of two-dimensional (2D) disc-shaped, state-insensitive optical traps (*27*). The trapping potentials are approximately harmonic, with an axial (*Z*) trapping frequency ν_Z of ~80 kHz and a radial (*X*-*Y*) frequency ν_R of ~600 Hz; the slight anharmonicity makes the spacings between the energy levels uneven. Axial and radial degrees of freedom are decoupled during the initial lattice loading and cooling. Under typical temperatures ($1\,\mu K < T_R < 7\,\mu K$, $T_Z \sim 2\,\mu K$), atoms are cooled to the motional ground state along the *Z* direction. In contrast, the radial modes are thermally populated. The SU(*N*) symmetric spin degree of freedom is encoded in the 10 nuclear spin states with quantum number m_I (Fig. 1A) and the pseudo–spin ½ orbital degree of freedom in the two lowest electronic (clock) states ($^1S_0$ and $^3P_0$, henceforth $|g\rangle$ and $|e\rangle$, respectively). Under typical atomic occupancies (≲ 20 atoms per disc), temperatures, and trap volume ($\propto T_R$), the mean interaction energy per particle is at least two orders of magnitude smaller than the single-particle vibrational spacing along any direction. The spectral resolution available with a laser of 1×10^{-16} stability (*28*) enables us to accurately probe these interactions while addressing individual nuclear spin levels.

SU(*N*) spin-orbital Hamiltonian in energy-space lattice

Under our operating conditions, the atomic interactions are insufficiently energetic to transfer atoms between the initially populated, slightly anharmonic motional eigenmodes. To first-order approximation, atoms remain frozen in these quantized motional levels and the quantum dynamics takes place only in the internal degrees of freedom (spin and orbital) (*21*, *29*, *30*), in a way analogous to localized atoms in real-space lattice trapping potentials. This approximation greatly simplifies the modeling of our system. Here, the large energy gap between the interaction energy and the single-particle vibrational spacing, along with the anharmonicity and nonseparability of the optical trapping potential provided by the Gaussian laser beam profile, lead to an energetic suppression of mode-changing collisions (*31*). Moreover, the *s*-wave and *p*-wave (Fig. 1B) interactions, which are responsible for the dynamics, provide nonlocal interactions when viewed within the energy-space lattice, as they couple atoms without being overly sensitive to the thermally populated motional levels. The decoupling between motional and internal degrees of freedom, combined with the sub-hertz spectral resolution of the stable laser, allows us to probe spin lattice models with effective long-range couplings in a nondegenerate Fermi gas, as schematically illustrated in Fig. 1C. This system thus paves the way for studies of quantum orbital magnetism beyond the ultracold regime.

Spin models with long-range interactions have been implemented in dipolar gases (*32*) or trapped ionic systems (*33*), but our system is further enriched by SU(*N*) symmetry and holds potential for addressing important open questions about many-body dynamics in spin-orbital models under the co-presence of large degeneracy (*13*, *34*, *35*) and long-range interactions. By performing Ramsey spectroscopy with various nuclear spin mixtures, we determine the nuclear spin independence of the *s*-wave and *p*-wave interactions. Furthermore, we probe the non-equilibrium dynamics of the orbital coherence, and the results are well reproduced by a two-orbital SU(*N*) spin lattice model in quantized motional eigenenergy space.

Interactions between two ^{87}Sr atoms are governed by Fermi statistics with an overall wave function antisymmetrization under exchange in the motional, electronic, and nuclear spin degrees of freedom (Fig. 1B). Consider a pair of interacting atoms (*j* and *k*) occupying two of the quantized

[1]JILA, National Institute of Standards and Technology and University of Colorado, Boulder, CO 80309, USA. [2]Department of Physics, University of Colorado, Boulder, CO 80309, USA. [3]Institute for Quantum Optics and Quantum Information of the Austrian Academy of Sciences, A-6020 Innsbruck, Austria. [4]Institute for Theoretical Physics, University of Innsbruck, A-6020 Innsbruck, Austria. [5]Department of Physics and Astronomy, University of Delaware, Newark, DE 19716, USA. [6]Joint Quantum Institute, National Institute of Standards and Technology and University of Maryland, College Park, MD 20742, USA.
*Corresponding author. E-mail: arey@jilau1.colorado.edu (A.M.R.); ye@jila.colorado.edu (J.Y.)

eigenmodes of the trapping potential, $\mathbf{n}_j$ and $\mathbf{n}_k$. If the atoms are in a nuclear spin symmetric state, they experience *s*-wave interactions only if their electronic state is antisymmetric: $(|eg\rangle - |ge\rangle)/\sqrt{2}$. We denote the elastic scattering length characterizing those collisions as a_{eg}^{-}. They can collide via *p*-wave interactions in three possible electronic symmetric configurations $\{|gg\rangle, |ee\rangle, (|eg\rangle + |ge\rangle)/\sqrt{2}\}$, corresponding to the *p*-wave elastic scattering lengths b_{gg}, b_{ee}, and b_{eg}^{+}, respectively. In contrast, if the two atoms are in an antisymmetric nuclear spin configuration, they experience *s*-wave collisions under these three electronic symmetric configurations, with the corresponding scattering lengths a_{gg}, a_{ee}, and a_{eg}^{+}, respectively. Similarly, *p*-wave interactions occur in $(|eg\rangle - |ge\rangle)/\sqrt{2}$, corresponding to the scattering length b_{eg}^{-}. These eight parameters characterize elastic collisions at ultralow temperatures, and SU(*N*) symmetry predicts them to be independent of the nuclear spin configuration.

The Hamiltonian that governs these interactions, between atoms *j* and *k*, can be written in terms of orbital-spin ½ operators $\hat{T}_j^{x,y,z}$ acting on the *j*-atom's electronic state, {*e*, *g*}, and in terms of nuclear-spin permutation operators $\hat{S}_n^m(j) = |n\rangle_j\langle m|$, acting on the *j*-atom's nuclear spin levels, $n, m \in \{1, 2, \ldots, N\}$ as

$$\hat{H}_{j,k} = (\hat{\mathcal{P}}^{+}\hat{H}^{+} + \hat{\mathcal{P}}^{-}\hat{H}^{-}) \quad (1)$$

and

$$\hat{H}^{\pm} = J_{j,k}^{\pm}\,\vec{T}_j \cdot \vec{T}_k + \chi_{j,k}^{\pm}\hat{T}_j^z\hat{T}_k^z + C_{j,k}^{\pm}\left(\frac{\hat{T}_j^z + \hat{T}_k^z}{2}\right) + K_{j,k}^{\pm}\hat{\mathbb{I}} \quad (2)$$

(*31*), where $\hat{\mathbb{I}}$ is the identity matrix, and

$$\hat{\mathcal{P}}^{\pm} = \frac{\left[\hat{\mathbb{I}} \pm \sum_{n,m=1}^{N}\hat{S}_n^m(j)\hat{S}_m^n(k)\right]}{2} \quad (3)$$

are nuclear spin projector operators into the symmetric triplet (+) and antisymmetric singlet (–) nuclear spin states, respectively. Equation 1 states that if the nuclear spin of the atoms is in (+) or (–), then they interact according to $\hat{H}^{+}$ or $\hat{H}^{-}$, respectively. The coupling constants $J_{j,k}^{\pm}, \chi_{j,k}^{\pm}, C_{j,k}^{\pm}, K_{j,k}^{\pm}$ depend on the scattering parameters a_η and b_η, $\eta \in \{ee, gg, eg^{+}, \text{and } eg^{-}\}$, and the wave function overlap of the radial vibrational modes of the *j*- and *k*-atoms in the 2D traps (*31*).

The total interaction Hamiltonian is the sum over all pairs of atoms, $\hat{H}^{SO} = \sum_{j>k}\hat{H}_{j,k}$, and commutes with all the SU(*N*) generators, $\hat{S}_n^m(j)$. $\hat{H}^{SO}$ is thus invariant under transformations from the SU(*N*) group [i.e., SU(*N*) symmetric]. This implies that the number of atoms in each of the nuclear spin sublevels is conserved. *N* is chosen by the initial state preparation of the nuclear spin distribution and can vary from 1 to $2I + 1 = 10$ in ^{87}Sr ($I = 9/2$). In this experiment, we control *N* via optical pumping through another electronic state.

In addition to elastic interactions, ^{87}Sr atoms exhibit inelastic collisions. Among those, however, only the *e*-*e* ones have been observed to give rise to measureable losses (*36*); we denote these two inelastic scattering lengths as γ_{ee} and β_{ee} for the *s*-wave and *p*-wave, respectively. We

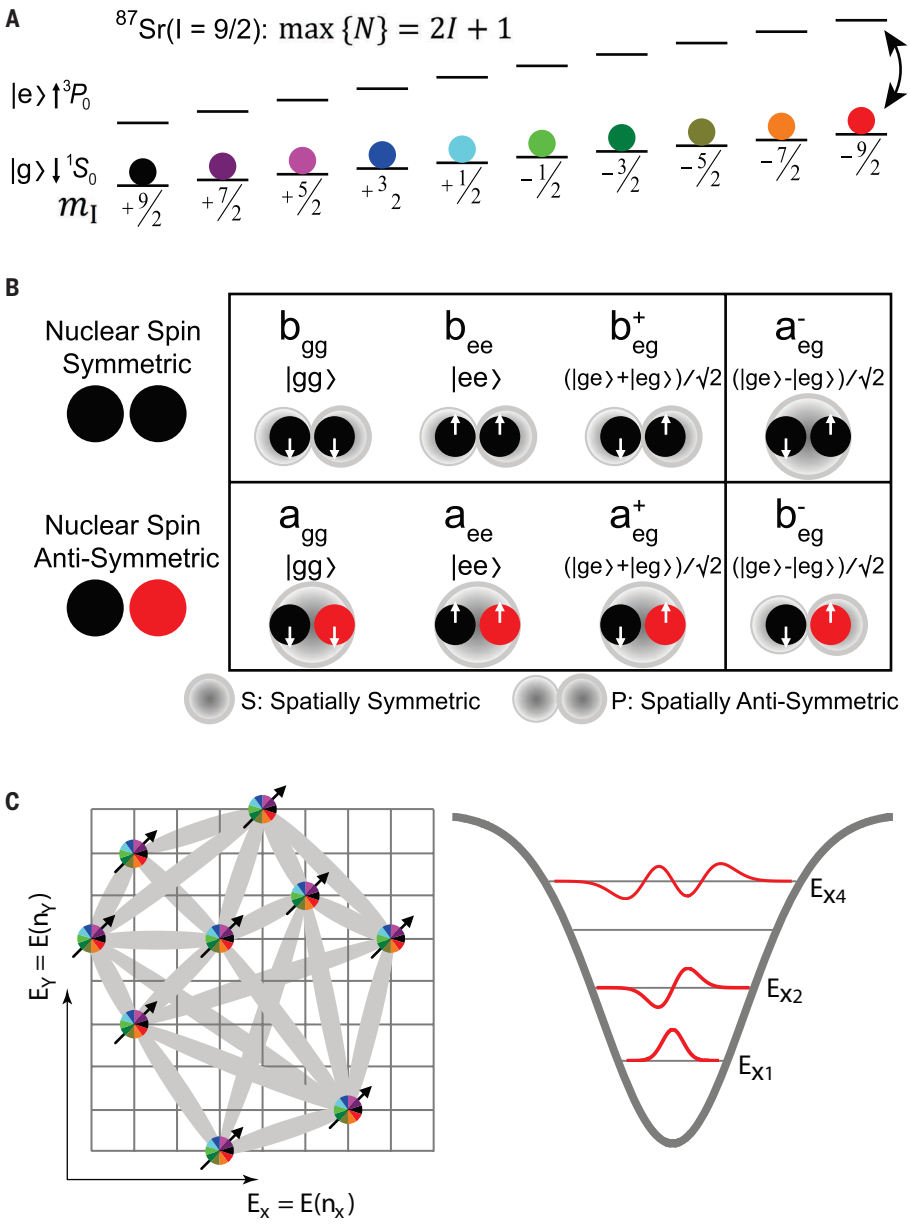

Fig. 1. Diagram of the interacting spin lattice. (**A**) Energy levels for the two lowest electronic states ($^1S_0$ and $^3P_0$) of ^{87}Sr atoms in a magnetic field, each with 10 nuclear spin states, depicted by colors. This color scheme is used in all figures to denote the interrogated state. (**B**) Interactions between two fermionic atoms characterized by four *s*-wave (*a*) and four *p*-wave (*b*) elastic scattering parameters. The interactions are governed by symmetries in motional states (bottom labels), nuclear spins (left labels), and electronic orbitals (white arrows). (**C**) Left panel: Schematics of the interacting electronic orbitals (spin-½ arrows) distributed over a lattice spanned by motional eigenenergies. In our system, the energy levels are populated according to a Boltzmann distribution and the energy spacings are slightly anharmonic; the latter is crucial for freezing atoms in their initially populated motional modes. For simplicity, neither the anharmonic lattice spacing, nor the Boltzmann population of modes are reflected in the figure. The shaded connections illustrate the long-range nature of the interactions in energy space. In our theoretical approach, those interactions are calculated using the matrix element overlap of the corresponding modes (*31*). To a first-order approximation, *p*-wave interactions can be treated collectively and can be assumed to be of all-to-all type. Thus, we can replace the values of the coupling constants with their thermal averages (*29*). Colored circles show the possibility of preparing statistical mixtures of *N* nuclear spin states. Right panel: Illustration of a few occupied eigenmodes in our optical trap formed by a Gaussian beam.

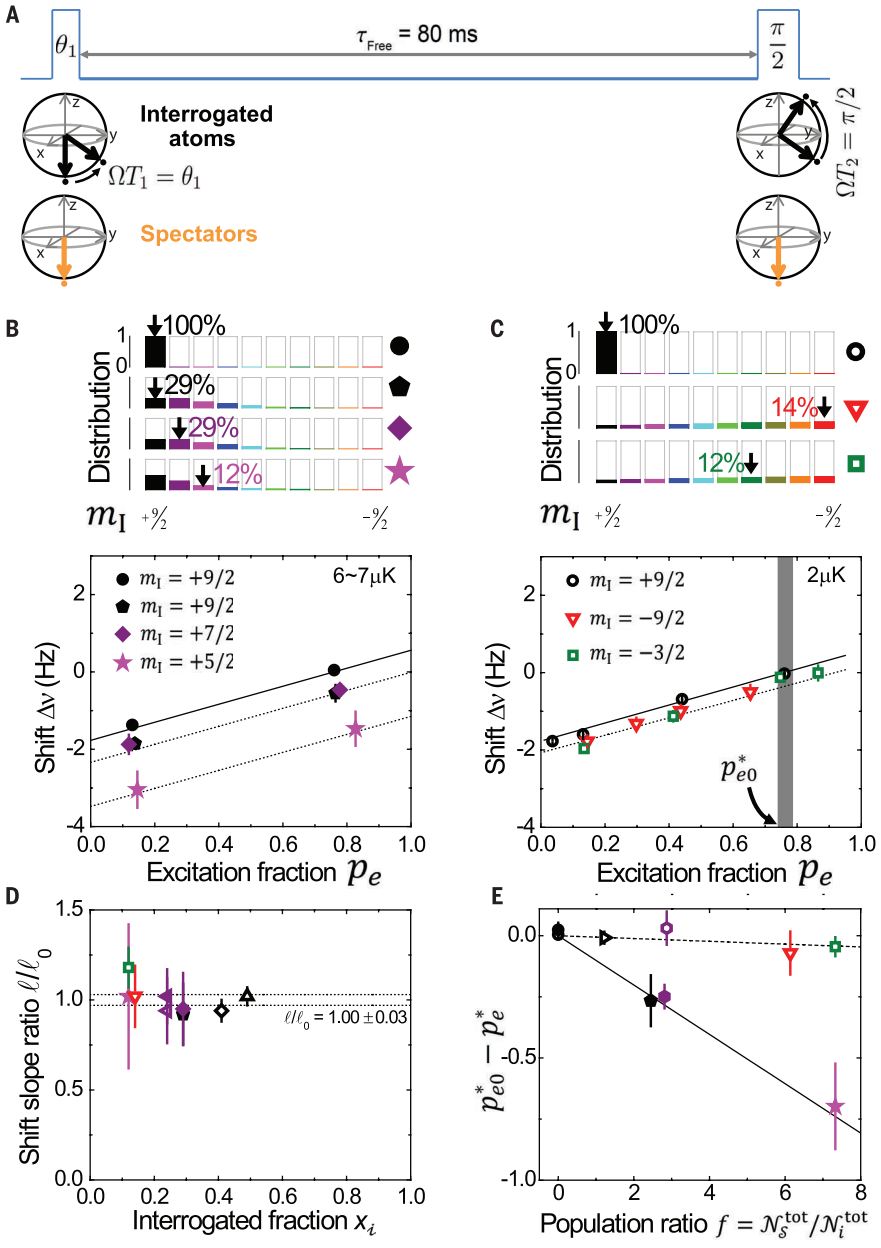

Fig. 2. Nuclear spin independence of interaction effects. (**A**) Ramsey sequence with an initial pulse of area θ_1, a final $\pi/2$ pulse, and a free evolution period τ_{free} = 80 ms. The spectator atoms remain in $|g\rangle$. (**B** and **C**) Upper panels: Illustration of the interrogated states (black arrows) and population distributions among various nuclear spin states. Lower panels: Measured density shifts (in symbols) for different nuclear spin configurations at (B) T_R = 6 to 7 μK and (C) ~2 μK. For consistency, the shifts are scaled for $\mathcal{N}_i^{tot}$ = 4000. The solid and dotted lines show theory calculations for the corresponding x_i and T_R as indicated in the plots, with b_{eg}^- and a_{eg}^- evaluated using the fitting parameter extracted from (E) and other remaining parameters determined from previous measurements (Table 1). The gray band in (C) corresponds to p^*_{e0}, the excitation fraction for zero density shift in a polarized sample. The spectator atoms generate a temperature-dependent density shift, which is independent of p_e of the interrogated atoms and thus manifests as a net offset from the purely polarized density shift. (**D**) Ratio of the slope of the frequency shift between the spin-mixed and spin-polarized samples. The dotted lines represent the standard error. (**E**) The difference in the zero-shift excitation fraction between the spin-mixed and spin-polarized samples. The solid and dashed lines are theory fits used to determine b_{eg}^- and consequently a_{eg}^- by the analytic relations between *s*- and *p*-wave scattering parameters (*31*). In (D) and (E), two values of T_R are used: 2.3 ± 0.2 μK (open symbols) and 6.5 ± 0.4 μK (solid symbols). In addition to conditions used for (B) and (C), other spin configurations are studied: open up triangles (x_i = 49%), open diamond (41%), open right triangles (46%), open and solid hexagons (26%), open and solid left triangles (24%), solid pentagons (29%), and solid stars (12%). Error bars represent 1σ multiplied by $\sqrt{\chi^2_{reduced}}$.

set other inelastic parameters to zero because of their negligible contributions in measurements (*36*).

Density-dependent frequency shift for nuclear spin mixtures

We first tested SU(*N*) symmetry in a two-orbital system by measuring the density-dependent frequency shift of the clock transition under various nuclear spin population distributions. We used a Ramsey sequence to measure interactions (*21*) under an external magnetic field that produces Zeeman splittings much larger than the interaction energy. The sequence starts with all atoms in $|g\rangle$ (Fig. 2A). Only atoms in a particular nuclear spin state are coherently excited and interrogated, whereas atoms in other states ("spectators") remain in $|g\rangle$. We denote the number of interrogated atoms by $\mathcal{N}_i^{tot}$, the number of spectator atoms by $\mathcal{N}_s^{tot}$, and define a population ratio $f = \mathcal{N}_s^{tot}/\mathcal{N}_i^{tot}$ and the interrogated fraction $x_i = \mathcal{N}_i^{tot}/(\mathcal{N}_i^{tot} + \mathcal{N}_s^{tot})$. We controlled the fraction of interrogated atoms excited to $|e\rangle$, p_e = $(1 - \cos\theta_1)/2$, by varying the initial pulse area θ_1, where $0 < \theta_1 < \pi$. After a free evolution time τ_{free} = 80 ms, a second pulse of area $\pi/2$ was applied for subsequent readout of the electronic orbital distributions. The resonance frequency shift was recorded as a function of the atomic number in the trap, which can be varied in a controlled manner. Interactions between atoms modify the resonance frequency in a density-dependent manner, and the measurement of this frequency gives us information about the interaction parameters.

We operate with highly homogeneous atom-laser coupling such that the orbital excitation is the same for all interrogated atoms. Consequently, in a fully spin-polarized sample, the *s*-wave interactions are suppressed and the *p*-wave interactions dominate the free evolution dynamics (*21*). The *s*-wave interactions are allowed only when spectator atoms populate other nuclear spin states. The existence of SU(*N*) symmetry in the scattering parameters results in an independence of the density shift with respect to both the interrogated nuclear spin state and the distribution of spectator atoms among the various spin components. Moreover, in the presence of a large magnetic field (which energetically suppresses excitation of the spectator atoms), the density shift should be only a function of $\mathcal{N}_i^{tot}$, p_e, and $\mathcal{N}_s^{tot}$.

In Fig. 2B, we compare the fully spin-polarized case (m_I = +9/2) against three other scenarios with different spin mixtures under T_R = 6 to 7 μK. The density shift is expected to be a linear function of p_e, arising from the fact that the *p*-wave interaction among $\mathcal{N}_i^{tot}$ has a quadratic dependence on the *z* component of the total orbital spin (*21*). When scaled to the same number of interrogated atoms ($\mathcal{N}_i^{tot}$ = 4000), the observed density shifts show three features: (i) The linear slope *l* depends only on $\mathcal{N}_i^{tot}$, (ii) the offset with respect to the polarized case increases linearly with *f*, and (iii) both *l* and the offset are independent of how the atoms are distributed in the nuclear

spin levels. The last point is verified, for example, by measuring the same shifts when interrogating 29% of the total population in either +9/2 or +7/2.

Temperature-dependent SU(*N*)-symmetric interactions

To determine the temperature dependence for the density shift and for additional confirmation of the observed nuclear spin independence, we interrogated other nuclear spin states, −9/2 or −3/2, at a lower $T_R \sim 2$ μK, when the distribution across all spin states is nearly even (Fig. 2C). The measured density shifts scaled to $\mathcal{N}_i^{tot} = 4000$ are again similar to each other, providing further direct experimental evidence for SU(N = 10) symmetry. At this lower T_R, the slope still depends only on $\mathcal{N}_i^{tot}$, but there is a smaller offset of the density shift relative to the polarized case when x_i varies. To quantify the T_R dependence, we plotted all measured ratios, l/l_0, where l_0 is the linear slope for the polarized case. We see that (I) the ratios collapse into a single value independently of f and T_R for fixed $\mathcal{N}_i^{tot}$, yielding $l/l_0 = 1.00 \pm 0.03$ (Fig. 2D). This result agrees well with the SU(N)-predicted ratio of unity and verifies this symmetry to the 3% level.

We emphasize that the test of two-orbital SU(N) symmetry (at the 3% level) is based directly on the measured interactions that are independent of nuclear spin configurations, and it does not require accurate knowledge of some common-mode system calibrations. For quantum simulations of SU(N) physics, it is important to precisely test this symmetry to a level much below all relevant energy scales. Although our measurement uncertainty (3%) has not reached the ultimate theoretical prediction (0.1%) resulting from a small admixture of the $^3P_0$ state with higher-lying P states with finite electronic angular momenta (*1*–*3*), it is already sufficient for realizing a SU(N)-symmetric, unity-filling spin lattice system (*31*). Further reduction in our experimental uncertainty can be achieved by enhancing the measurement precision with improved laser stability. We observe that l decreases by only 10% when T_R is raised from 2 μK to 6 μK, verifying its low sensitivity to T_R as expected for p-wave interactions in 2D systems.

We also determined the excitation fraction where the shift is zero for a spin mixture, p_e^*, and compare it to that of a polarized sample, p_{e0}^* (gray bands, Fig. 2C), for various interrogated spin states (colors in Fig. 2E). The difference shows the following features: (II) It collapses onto a single line (for a given T_R of either 2.3 or 6.5 μK) as a function of f, which provides further evidence for the spin independence of the interactions; (III) at $\mathcal{N}_s^{tot} = 0$ (fully polarized), the two lines cross each other at the origin, as expected from the T_R insensitivity of the p-wave interactions. The proportionality constant of $(p_{e0}^* - p_e^*)$ to f is finite for 6.5 μK (lower line) and decreases to almost zero for $T_R \sim 2.3$ μK (upper line). This near-zero proportionality constant for $T_R \sim 2.3$ μK reflects an accidental cancellation of the spectators' s- and p-wave interaction effects at this temperature.

Experiment-theory agreement and determination of the scattering parameters

In the presence of a large external magnetic field that produces differential Zeeman splittings much larger than the interaction energy, those terms in the Hamiltonian that exchange the population between the occupied spin-orbital levels are energetically suppressed and the populations of different spin-orbital levels are conserved. Hence, the Hamiltonian is dominated by Ising-type interactions that preserve the spin-orbital population. In this regime, the many-body dynamics for a single lattice site with $\mathcal{N}$ atoms can be captured under a collective approximation that replaces the coupling constants with their corresponding thermal averages, $O^{\pm}_{\mathbf{n}j,\mathbf{n}k} \to \overline{O}^{\pm}$ (*29*). For the experimentally relevant case where only $\mathcal{N}_i$ atoms in spin m_I are interrogated and where $\mathcal{N}_s$ atoms in the other spin components remain in $|g\rangle$, the effective many-body Hamiltonian during τ_{free} simplifies substantially. It consists of two parts, $\hat{H}^{SO} = \hat{H}_i + \hat{H}_s$. The first part, $\hat{H}_i = \overline{\chi}^+(\hat{\mathbb{T}}^z)^2 + \overline{C}^+\hat{\mathbb{T}}^z\mathcal{N}_i$, describes the p-wave interactions between the interrogated atoms (*21*, *29*), where $\hat{\mathbb{T}}^{\alpha=x,y,z} = \sum_j^{\mathcal{N}} \hat{S}_{m_I}^{m_I}(j)\hat{T}_j^{\alpha=x,y,z}$ are collective orbital operators acting on the $\mathcal{N}_i$ interrogated atoms. The density shift induced by these interactions, $\Delta\nu^i = \mathcal{N}_i(\overline{C}^+ - \cos\theta_1\overline{\chi}^+)$, with $\overline{\chi}^+ = [(b_{ee}^3 + b_{gg}^3 - 2b_{eg}^{+3})/2]\langle P\rangle_{T_R}$ and $\overline{C}^+ = [(b_{ee}^3 - b_{gg}^3)/2]\langle P\rangle_{T_R}$, depends linearly on the number of excited atoms $\mathcal{N}_i p_e$. Here, $\langle P\rangle_{T_R}$ corresponds to the thermal average of the p-wave mode overlap coefficients. Assuming a Boltzmann distribution of initially populated radial motional modes, we have $\langle P\rangle_{T_R} \propto (T_R)^0$ (insensitive to T_R) (*21*). For a spin-polarized sample, the observed density shifts are well reproduced by theory (solid black lines in Fig. 2, B and C) based on the same p-wave parameters as determined in (*21*). The second part, $\hat{H}_s = \mathcal{N}_s\overline{\Lambda}\,\hat{\mathbb{T}}^z$, describes the interactions between the interrogated and spectator atoms with both p- and s-wave contributions. The related density shift is $\Delta\nu^s = \overline{\Lambda}\,\mathcal{N}_s$, with

$$\overline{\Lambda} = \frac{\overline{C}^+ + \overline{C}^- - \overline{J}^+ - \overline{J}^- - \overline{\chi}^+ - \overline{\chi}^-}{2} = \frac{a_{eg}^+ + a_{eg}^- - 2a_{gg}}{4}\langle S\rangle_{T_R} + \frac{b_{eg}^{+3} + b_{eg}^{-3} - 2b_{gg}^3}{4}\langle P\rangle_{T_R} \quad (4)$$

The s-wave thermal average, $\langle S\rangle_{T_R}$, decreases with T_R as $\langle S\rangle_{T_R} \propto (T_R)^{-1}$. So far we have focused on a single lattice site. To compare with the experimental results, we perform averaging over the atom distributions across all lattice sites. Consequently, the density shifts $\Delta\nu^s$ and $\Delta\nu^i$ become proportional to $\mathcal{N}_s^{tot}$ and $\mathcal{N}_i^{tot}$, respectively.

This model fully reproduces the experimental observations as summarized in points (i) to (iii) and (I) to (III) above and shown in Fig. 2. To quantitatively compare with the experiment, we performed a Poissonian average of the atom number across the array of 2D traps and used the average excitation fraction to account for the two-body e-e losses (*21*, *36*) during τ_{free}. The capability of the SU(N) spin lattice model to reproduce the experimental observations also enabled us to determine the remaining s- and p-wave scattering parameters. For each of the four channels, $\eta \in \{ee, gg, eg^+, eg^-\}$, the s-wave and p-wave parameters relate to each other through the characteristic length, $\bar{a}_\eta$, of the van der Waals potential (*37*). Thus, after we determined $\bar{a}_\eta$ using the available van der Waals C_6 coefficients (*31*), only four elastic scattering parameters remained independent. Among those, a_{gg}, b_{ee}, and b_{eg}^+ (and thus their respective p- or s-wave counterparts) are known (*21*), leaving only one unknown parameter associated with the eg^- channel. Using the theoretical predictions and a single parameter to fit the data in Fig. 2E, we extracted values for a_{eg}^- and b_{eg}^-. Table 1 lists all the scattering parameters determined from the prior and current measurements.

Coherent dynamic spectroscopy

We performed coherent dynamic spectroscopy to explore the development of many-body correlations as a key effect of Ising orbital magnetism, in the combined orbital and nuclear spin degrees of freedom, generated by the p-wave and s-wave interactions. This allowed us to further validate the SU(N) spin-orbital model (Eq. 1) as a description for our system. The many-body correlations that build up during the free evolution manifest as a decay of the e-g orbital coherence in the form of Ramsey fringe contrast $\mathcal{C}(\tau_{free}) = 2/\mathcal{N}_i^{tot}\sqrt{\langle\hat{\mathbb{T}}_{tot}^x\rangle^2 + \langle\hat{\mathbb{T}}_{tot}^y\rangle^2}$ that we measure as a function of τ_{free}. Here, $\hat{\mathbb{T}}_{tot}^{x,y}$ is the sum of $\hat{\mathbb{T}}^{x,y}$ over the 2D traps. We extracted a normalized value of $\mathcal{C}$ by comparing the high-atom-number raw contrast against that of the low atom number; this normalization removes single-particle decoherence effects. The decay of $\mathcal{C}$ during the free-evolution period has been shown to be a particularly suitable observable for characterizing the role of interactions during the dynamics (*38*). For example, contrast measurements in an array of polar molecules pinned in a 3D lattice provided clear signatures of dipolar interactions and their description in terms of a spin exchange model (*32*, *39*).

In the presence of a large magnetic field, the decay of $\mathcal{C}$ has two sources. The first arises from within the interrogated atoms: p-wave elastic interactions, two-body e-e losses, higher-order interaction-induced mode-changing processes, as well as dephasing induced by the distribution of atoms across traps. All these p-wave effects are accounted for in our theory using the same p-wave parameters that were determined in (*21*) and then reconfirmed with our density shift measurements in this work (Fig. 2). The second source comes from spectators, which act on the interrogated atoms at a given site as an inhomogeneous and density-dependent effective magnetic field

Table 1. *s*- and *p*-wave scattering lengths in units of the Bohr radius. Here, except for a_{gg} = 96.2 ± 0.1 a_0, all the other scattering parameters are extracted in this work on the basis of current (this work) and previous measurements (*21*, *36*) as well as the analytic relations (*37*).

Channel	Scattering lengths in units of the Bohr radius (a_0)		Determination method
	s-wave	*p*-wave	
gg	96.2 ± 0.1	74.6 ± 0.4	*s*-wave: Two-photon photoassociative spectroscopy (*25*) and rovibrational spectroscopy (*26*) *p*-wave: Analytic relation between *s*- and *p*-wave parameters (*37*)
eg^+	169 ± 8	−169 ± 23	*s*-wave: Analytic relation (*37*) *p*-wave: Density shift in a polarized sample (*21*)
eg^-	68 ± 22	-42^{+103}_{-22}	*s*-wave: Density shift in a spin mixture at different temperatures (this work) *p*-wave: Analytic relation (*37*)
ee (elastic)	176 ± 11	−119 ± 18	*s*-wave: Analytic relation (*37*) *p*-wave: Density shift in a polarized sample (*21*)
ee (inelastic)	$\gamma_{ee} = 46^{+19}_{-32}$	β_{ee} = 121 ± 13	Two-body loss measurement (*36*) and analytic relation (*37*)

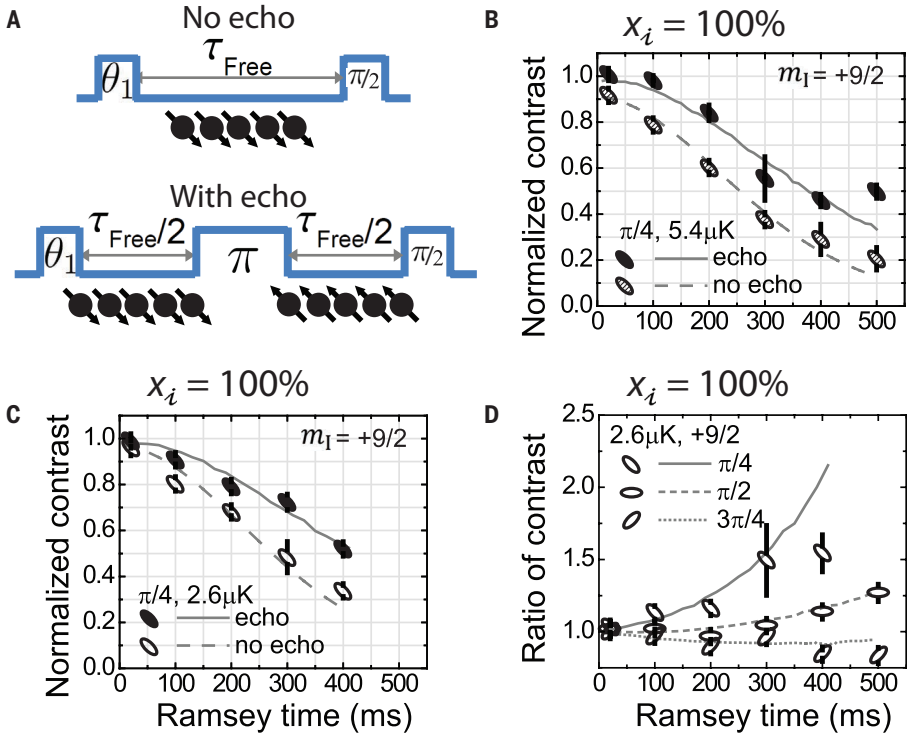

Fig. 3. Evolution of orbital coherence in nuclear spin-polarized samples. (**A**) Upper panel: Ramsey sequence with varying θ_1 and τ_{free}. Lower panel: Sequence with an echo (π) pulse. The group of circles illustrates the orbital configurations for interrogated atoms (black circles). (**B** and **C**) Normalized Ramsey contrasts for $\theta_1 = \pi/4$, $x_i = 100\%$, under two different radial temperatures, T_R = 5.4 μK and 2.6 μK, respectively. The contrast is normalized by comparing the high-atom-number raw Ramsey fringe contrast, $\mathcal{C}$ (defined in the main text), against the low-atom-number raw contrast. The high total atom numbers (measured at a very short free evolution time, τ_{free} = 20 ms) are in the range of 2200 to 3100 for Figs. 3 and 4 (day-to-day variation over 4 months). However, for each specific case, the data without and with echo were taken on the same day and their atom numbers are matched to within 3 to 7%. These atom numbers are recorded and serve as inputs to our theory calculation of Ramsey contrast decay. Solid and open symbols denote measurements with and without echo; solid and dashed lines show theory calculations with and without echo, respectively, using a two-orbital model with independently determined parameters (based on measurements shown in Fig. 2 and previous studies, see Table 1). Under the conditions of (B) and (C), the dominant source for contrast decay arises from *p*-wave interactions between the interrogated atoms. (**D**) Effects of echo, characterized by the ratio of contrast with echo to that without echo, for $\theta_1 = \pi/4$ (antidiagonal ellipse and solid line), $\pi/2$ (horizontal ellipse and short dashed line), and $3\pi/4$ (diagonal ellipse and short dotted line), under x_i = 100%. Error bars represent 1σ multiplied by $\sqrt{\chi^2_{reduced}}$.

along *z*, with both *s*- and *p*-wave contributions. The effective magnetic field is static if the atoms are frozen in their motional states, but can vary with time in the presence of higher-order mode-changing processes. The *p*-wave interaction plays a dominant role at high T_R = 5 to 6 μK, whereas the *s*-wave interaction, which has a stronger dependence on the mode distribution, becomes important at lower T_R. We focus first on the nuclear spin-polarized case (Fig. 3) to benchmark our model, and then use various population distributions among nuclear spin states to investigate the interplay between orbital and spin degrees of freedom (Fig. 4).

Two-orbital dynamics in spin-polarized atoms

To understand in detail the orbital dynamics induced by *p*-wave interactions, we first studied a nuclear spin polarized sample (x_i = 100%) for T_R = 5 to 6 μK and $\theta_1 = \pi/4$ (Fig. 3B). To separate the effects of dephasing and many-body correlation in the contrast decay, we applied a π echo pulse in the middle of the Ramsey sequence (Fig. 3A, lower panel). The π echo pulse modifies the contrast decay in a θ_1-dependent way because of the enhanced *e*-*e* loss after the echo pulse (note the number normalization in $\mathcal{C}$) for $\theta_1 < \pi/2$, as well as because the *p*-wave contribution to contrast decay contains both θ_1-independent and θ_1-dependent terms. The θ_1-independent contribution is generated by the term $\bar{C}^+\hat{\mathbb{T}}^z\mathcal{N}_i$. This term is responsible for the density-dependent dephasing between atoms distributed in different 2D traps. The echo pulse removes it as well as other dephasing effects of technical origin. The θ_1-dependent contribution is generated by the term $\bar{\chi}^+(\hat{\mathbb{T}}^z)^2$ in the Hamiltonian and can lead to many-body orbital correlations that are not removable by echo.

For $\theta_1 = \pi/4$, the Ramsey contrast decays more slowly with an echo pulse (Fig. 3B). This positive echo effect can be attributed to the suppressed dephasing from inhomogeneous atomic densities across different 2D traps (θ_1-independent contribution) and to the faster number loss with echo (as we normalize the contrast against remaining atom number).

In a polarized sample where *p*-wave interactions dominate, the contrast decay is expected to be insensitive to T_R. This is confirmed with measurements performed at T_R = 2.6 μK (Fig. 3C) that show similar decay behaviors to those at 5.4 μK (Fig. 3B). In addition, we find an excellent agreement between the data and the theoretical model that uses temperature-insensitive *p*-wave parameters. Figure 3D plots the ratio of contrasts with and without echo for different pulse areas and illustrates the positive echo effect in suppressing contrast decay for $\theta_1 = \pi/4$, as well as the negative effect for $\theta_1 = 3\pi/4$ when the echo enhances contrast decay. The negative echo effect can be attributed to both the development of many-body orbital correlations for $\theta_1 = 3\pi/4$ (*21*) and the reduced *e-e* loss after the echo. All measurements are well reproduced by our spin lattice model.

Spin-orbital SU(*N*) dynamics in spin mixtures

To investigate the interplay between orbital and spin degrees of freedom, we performed similar spectroscopic measurements in spin-mixed samples (Fig. 4A). We studied the spin-mixed cases under T_R = 5 to 6 μK, with $\theta_1 = \pi/4$ and the interrogated fraction x_i = 14% and 56% (Fig. 4, B and C, respectively). Here, the data show similar positive effect of an echo pulse in the presence of spectator atoms. Because *p*-wave interactions between interrogated atoms are reduced as the interrogated fraction decreases, the overall contrast decay becomes slower. On the basis of the determined scattering parameters, our model predicts that spectator atoms cause almost negligible decoherence effects at this high T_R = 5 to 6 μK (*31*).

When we decreased T_R to ~2 μK, the rise of the *s*-wave contribution caused enhanced decoherence effects coming from the spectator atoms. Figure 4D illustrates the influence of spectators for the x_i = 14% minority case, where contrast decay is clearly faster than in Fig. 4B. The inclusion of off-resonant mode-changing collisions as higher-order corrections is required for temperatures below 5 μK to accurately reproduce the experimental observations (*31*). These mode-changing collisions can be visualized as relocating pairs of atoms in the energy-space lattice shown in Fig. 1C, analogous to interaction-induced tunneling processes in a real-space lattice. The echo pulse suppresses the part of contrast decay arising from mode-preserving collisions between spectators and interrogated atoms, but it cannot reverse the decay due to mode-changing processes. In Fig. 4D, the measured contrast decay with echo enables us to determine a single parameter characterizing the mode-changing processes (*31*).

For a further and independent test of our model, we explored another case with x_i = 56% and T_R ~ 2 μK, such that both the interrogated atoms and spectator atoms have important contributions to the contrast decay. The data were well described by the same theory model (Fig. 4E and fig. S1) without any variation of the predetermined parameters, demonstrating a firm understanding of the system dynamics.

The experimental exploration of exotic SU(*N*) physics is just starting. The unique capability of precision laser spectroscopy has so far allowed us to explore Ising orbital magnetism at relatively high temperatures. Future studies will explore the full Hamiltonian including the exchange interactions by controlling the atomic density, temperature, and the magnetic field to engineer various spin-spin and spin-orbital dynamics. This will allow expansion of the frontier of emergent many-body quantum physics at increasingly high temperatures, as well as the study of time-resolved dynamics in the SU(*N*) Kondo lattice and Kugel-Khomskii models (*3*, *40*, *41*) in the quantum gas regime.

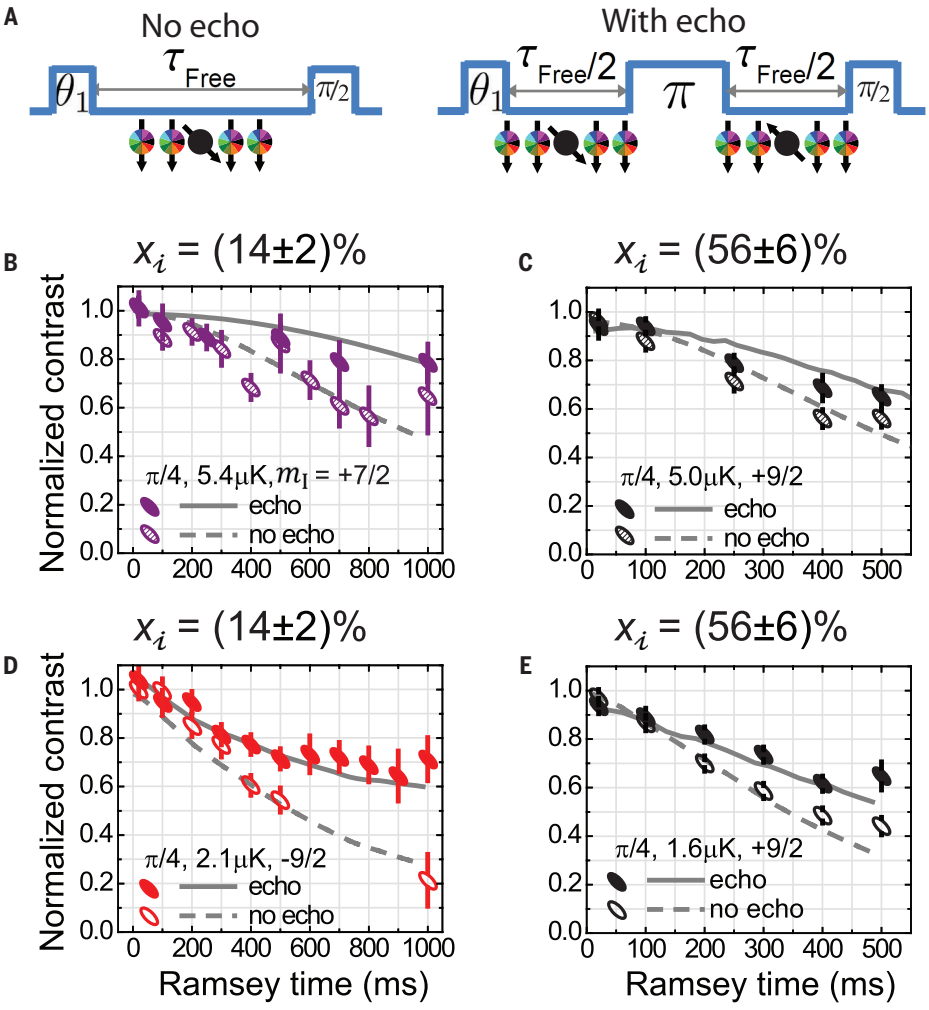

Fig. 4. Evolution of orbital coherence in nuclear spin-mixed samples. (**A**) Left panel: Ramsey sequence with varying θ_1 and τ_{free}. Right panel: Sequence with an echo (π) pulse. The group of circles illustrates the orbital configurations for interrogated atoms (black circles) and spectator atoms (colored circles). (**B** and **D**) Normalized Ramsey contrast for $\theta_1 = \pi/4$, $x_i = 14 \pm 2\%$, under T_R = 5.4 μK and 2.1 μK, respectively: measurements with echo (solid symbols) and without echo (open symbols). (**C** and **E**) Normalized contrast for $\theta_1 = \pi/4$, $x_i = 56 \pm 6\%$, under T_R = 5.0 μK and 1.6 μK, respectively. Solid and dashed lines show theory calculations with and without echo, respectively, using a two-orbital model with independently determined parameters (based on measurements shown in Fig. 2 and previous studies, see Table 1). In this model, the spectators act as an effective inhomogeneous magnetic field causing dephasing to the interrogated atoms. Without mode-changing collisions, the dephasing is static and removable by echo; with mode-changing collisions, it is assumed and confirmed experimentally that echo does not remove the time-dependent dephasing. The theory uses a single fitting parameter for the mode-changing processes for all plots. Error bars represent 1σ multiplied by $\sqrt{\chi^2_{reduced}}$.

REFERENCES AND NOTES

1. M. M. Boyd *et al.*, *Science* **314**, 1430–1433 (2006).
2. M. M. Boyd *et al.*, *Phys. Rev. A* **76**, 022510 (2007).
3. A. V. Gorshkov *et al.*, *Nat. Phys.* **6**, 289–295 (2010).
4. M. A. Cazalilla, A. F. Ho, M. Ueda, *New J. Phys.* **11**, 103033 (2009).
5. C. Wu, J. P. Hu, S. C. Zhang, *Phys. Rev. Lett.* **91**, 186402 (2003).
6. M. Hermele, V. Gurarie, A. M. Rey, *Phys. Rev. Lett.* **103**, 135301 (2009).
7. B. J. Bloom *et al.*, *Nature* **506**, 71–75 (2014).
8. A. J. Daley, M. M. Boyd, J. Ye, P. Zoller, *Phys. Rev. Lett.* **101**, 170504 (2008).
9. A. V. Gorshkov *et al.*, *Phys. Rev. Lett.* **102**, 110503 (2009).
10. A. J. Daley, *Quantum Inf. Process* **10**, 865–884 (2011).
11. I. Reichenbach, I. H. Deutsch, *Phys. Rev. Lett.* **99**, 123001 (2007).
12. D. Banerjee *et al.*, *Phys. Rev. Lett.* **110**, 125303 (2013).
13. Y. Tokura, N. Nagaosa, *Science* **288**, 462–468 (2000).

14. X. G. Wen, F. Wilczek, A. Zee, . *Phys. Rev. B* **39**, 11413–11423 (1989).
15. S. Kraft, F. Vogt, O. Appel, F. Riehle, U. Sterr, *Phys. Rev. Lett.* **103**, 130401 (2009).
16. S. Stellmer, F. Schreck, T. C. Killian, *Degenerate Quantum Gases of Strontium: Annual Review of Cold Atoms and Molecules, Vol. 2* (World Scientific, Singapore, 2014).
17. Y. Takasu *et al*., *Phys. Rev. Lett.* **91**, 040404 (2003).
18. S. Stellmer, R. Grimm, F. Schreck, *Phys. Rev. A* **84**, 043611 (2011).
19. S. Blatt *et al*., *Phys. Rev. Lett.* **107**, 073202 (2011).
20. R. Yamazaki, S. Taie, S. Sugawa, Y. Takahashi, *Phys. Rev. Lett.* **105**, 050405 (2010).
21. M. J. Martin *et al*., *Science* **341**, 632–636 (2013).
22. After submission of this work, we became aware of two independent studies of SU(*N*) physics in Yb atoms (*42*, *43*).
23. S. Taie, R. Yamazaki, S. Sugawa, Y. Takahashi, *Nat. Phys.* **8**, 825–830 (2012).
24. G. Pagano *et al*., *Nat. Phys.* **10**, 198–201 (2014).
25. Y. N. Martinez de Escobar *et al*., *Phys. Rev. A* **78**, 062708 (2008).
26. A. Stein, H. Knöckel, E. Tiemann, *Eur. Phys. J. D* **57**, 171–177 (2010).
27. A. D. Ludlow *et al*., *Science* **319**, 1805–1808 (2008).
28. T. L. Nicholson *et al*., *Phys. Rev. Lett.* **109**, 230801 (2012).
29. A. M. Rey *et al*., *Ann. Phys.* **340**, 311–351 (2014).
30. A. P. Koller, M. Beverland, A. V. Gorshkov, A. M. Rey, *Phys. Rev. Lett.* **112**, 123001 (2014).
31. See supplementary materials on *Science* Online.
32. B. Yan *et al*., *Nature* **501**, 521–525 (2013).
33. R. Islam *et al*., *Science* **340**, 583–587 (2013).
34. K. I. Kugel, D. I. Khomskii, *Sov. Phys. Usp.* **25**, 231–256 (1982).
35. P. Corboz, M. Lajkó, A. M. Läuchli, K. Penc, F. Mila, *Phys. Rev. X* **2**, 041013 (2012).
36. M. Bishof *et al*., *Phys. Rev. A* **84**, 052716 (2011).
37. Z. Idziaszek, P. S. Julienne, *Phys. Rev. Lett.* **104**, 113202 (2010).
38. K. R. A. Hazzard *et al*., http://arxiv.org/abs/1406.0937 (2014).
39. K. R. A. Hazzard *et al*., http://arxiv.org/abs/1402.2354 (2014).
40. M. Foss-Feig, M. Hermele, A. M. Rey, *Phys. Rev. A* **81**, 051603(R) (2010).
41. M. Hermele, V. Gurarie, *Phys. Rev. B* **84**, 174441 (2011).
42. F. Scazza *et al*., http://arxiv.org/abs/1403.4761 (2014).
43. G. Cappellini *et al*., http://arxiv.org/abs/1406.6642 (2014).

ACKNOWLEDGMENTS

We thank P. Julienne, B. Gadway, T. Nicholson, B. Bloom, and A. V. Gorshkov for technical discussions. Supported by the National Defense Science and Engineering Graduate Fellowship program and the NSF Graduate Research Fellowship program (M.B.) and by NIST, NSF grant PFC-1125844, Air Force Office of Scientific Research (MURI and single investigator award), Defense Advanced Research Projects Agency (QuASAR), Austrian Science Foundation, SFB FoQus (Foundations and Applications of Quantum Science), European Research Council Synergy Grant (UQUAM), and Simulators and Interfaces with Quantum Systems (SIQS) project. The data described in the paper are archived in a database at JILA.

SUPPLEMENTARY MATERIALS

www.sciencemag.org/content/345/6203/1467/suppl/DC1
Materials and Methods
Supplementary Text
Figs. S1 and S2
Tables S1 to S3
References (*44*–*58*)

18 April 2014; accepted 11 August 2014
Published online 21 August 2014;
10.1126/science.1254978

STRUCTURAL BIOLOGY

Crystal structure of the CRISPR RNA–guided surveillance complex from *Escherichia coli*

Ryan N. Jackson,[1] Sarah M. Golden,[1] Paul B. G. van Erp,[1] Joshua Carter,[1] Edze R. Westra,[2]* Stan J. J. Brouns,[2] John van der Oost,[2] Thomas C. Terwilliger,[3] Randy J. Read,[4] Blake Wiedenheft[1]†

Clustered regularly interspaced short palindromic repeats (CRISPRs) are essential components of RNA-guided adaptive immune systems that protect bacteria and archaea from viruses and plasmids. In *Escherichia coli*, short CRISPR-derived RNAs (crRNAs) assemble into a 405-kilodalton multisubunit surveillance complex called Cascade (CRISPR-associated complex for antiviral defense). Here we present the 3.24 angstrom resolution x-ray crystal structure of Cascade. Eleven proteins and a 61-nucleotide crRNA assemble into a seahorse-shaped architecture that binds double-stranded DNA targets complementary to the crRNA-guide sequence. Conserved sequences on the 3′ and 5′ ends of the crRNA are anchored by proteins at opposite ends of the complex, whereas the guide sequence is displayed along a helical assembly of six interwoven subunits that present five-nucleotide segments of the crRNA in pseudo–A-form configuration. The structure of Cascade suggests a mechanism for assembly and provides insights into the mechanisms of target recognition.

Clustered regularly interspaced short palindromic repeat (CRISPR) loci provide the molecular memory of an adaptive immune system that is prevalent in bacteria and archaea (*1*–*5*). Each CRISPR locus consists of a series of short repeats separated by nonrepetitive spacer sequences acquired from foreign genetic elements such as viruses and plasmids. CRISPR loci are transcribed, and the long primary transcripts are processed into a library of short CRISPR-derived RNAs (crRNAs) that contain sequences complementary to previously encountered invading nucleic acids. CRISPR-associated (Cas) proteins bind each crRNA, and the resulting ribonucleoprotein complexes target invading nucleic acids complementary to the crRNA guide. Targets identified as foreign are subsequently degraded by dedicated nucleases.

Phylogenetic and functional studies have identified three main CRISPR-system types (I, II, and III) and 11 subtypes (IA to IF, IIA to IIC, and IIIA to IIIB) (*6*). The type IE system from *Escherichia coli* K12 consists of a CRISPR locus and eight *cas* genes (Fig. 1A). Five of the *cas* genes in this system encode for proteins that assemble with the crRNA into a large complex called Cascade (CRISPR-associated complex for antiviral defense) (*7*). Efficient detection of invading DNA relies on complementary base pairing between the DNA target and crRNA-guide sequence, as well as recognition of a short sequence motif immediately adjacent to the target called a protospacer-adjacent motif (PAM) (*8*–*10*). Target recognition by Cascade triggers a conformational change and recruits a trans-acting nuclease-helicase (Cas3) that is required for destruction of an invading target (*8*, *11*–*15*). However, an atomic-resolution understanding of Cascade assembly and crRNA-guided surveillance has not been available.

To understand the mechanism of crRNA-guided surveillance by Cascade, we determined the 3.24 Å–resolution x-ray crystal structure of the complex (Fig. 1). The structure explains how the 11 proteins assemble with the crRNA into an interwoven architecture that presents discrete segments of the crRNA for complementary base pairing. Overall, the Cascade structure reveals features required for complex assembly and provides insights into the mechanisms of target recognition.

Overview of the Cascade structure

We determined the x-ray crystal structure of Cascade by molecular replacement, using the 8 Å cryo-electron microscopy (cryo-EM) map as a search model (Fig. 1, fig. S1, table S1, and supplementary materials and methods) (*12*). Initial phases were improved and extended to 3.24 Å by averaging over noncrystallographic symmetry (*16*). The asymmetric unit contains two copies of Cascade that superimpose with an average root mean square deviation (RMSD) of 1.29 Å for equivalently positioned Cα atoms (fig. S2). Here we focus our description on complex one, but both assemblies consist of 11 protein subunits and a single 61–nucleotide (nt) crRNA that traverses the length of the complex. Nine of the 11 Cas proteins make direct contact with the crRNA, and eight of the nine RNA-binding proteins contain a modified RNA recognition motif (RRM) (Fig. 1, B to D). The 5′ and 3′ ends of the crRNA are derived from the repeat region of the crRNA and are bound at opposite ends of the seahorse-shaped

[1]Department of Microbiology and Immunology, Montana State University, Bozeman, MT 59717, USA. [2]Laboratory of Microbiology, Department of Agrotechnology and Food Sciences, Wageningen University, Dreijenplein 10, 6703 HB Wageningen, Netherlands. [3]Bioscience Division, Los Alamos National Laboratory, Los Alamos, NM 87545, USA. [4]Department of Haematology, University of Cambridge, Cambridge Institute for Medical Research, Cambridge CB2 0XY, UK.
*Present address: Environment and Sustainability Institute, University of Exeter, Penryn Campus, Penryn, Cornwall TR10 9FE, UK. †**Corresponding author. E-mail: bwiedenheft@gmail.com**